Journal of Materials Chemistry B

ROYAL SOCIETY OF CHEMISTRY

PAPER

View Article Online
View Journal | View Issue

Cite this: J. Mater. Chem. B, 2025, 13, 14091

Engineering fluorescent probes for tracking lysosomal pH in β-amyloid-induced microglial activation and phagocytosis

Subrata Munan, †*[a] Abir Mondal,[b] Shraddha Tiwari,[a] Rashmi Yadav,[a] Niharika Pareek[a] and Animesh Samanta *[a]

Alzheimer's disease (AD) is primarily associated with the aggregation of amyloid-β (Aβ) due to insufficient clearance of Aβ peptides. This leads to deposition of fibrillar Aβ (fAβ), contributing to AD progression. Microglia, the brain's resident immune cells, are central to the phagocytotic-fusion of fAβ. Notably, fAβ itself can activate microglia *via* toll-like receptor signaling, triggering a phagocytic response. Previous studies have shown that activated microglia exhibit efficient phagocytotic-fusion of fAβ, primarily through lysosomal acidification compared to resting microglia. Therefore, distinguishing microglial activation states is vital for understanding and potentially modulating Aβ clearance mechanisms in AD. Herein, we systematically modified the structure to develop fluorescent probes (FPs), **PS-Mor** and **PM-DMor** based on morpholine-conjugated pyrylium and pyridinium derivatives of indigenous "IndiFluors". These probes exhibit strong fluorescence enhancement in lysosomal pH windows by modulating photoinduced electron transfer (PET). The turn-on behavior of the probes was further supported by TD-DFT/PCM theoretical calculations. Confocal imaging revealed that **PM-DMor** selectively localizes to lysosomes, while **PS-Mor** targets mitochondria in activated human microglia. **PM-DMor** effectively monitors intracellular pH changes (ΔpHi) during drug-induced apoptosis and discriminates activated from resting microglial using both fluorescence microscopy and flow cytometry. Importantly, **PM-DMor** also tracks Aβ-induced microglial activation and subsequent phagocytosis of Aβ. Overall, **PM-DMor** offers a valuable tool for probing lysosomal dynamics in microglia and holds promise for early-stage therapeutic strategies targeting Aβ clearance in Alzheimer's disease.

Received 25th April 2025,
Accepted 26th August 2025

DOI: 10.1039/d5tb00968e

rsc.li/materials-b

Introduction

The discrimination of cell state phenotypes is crucial in basic biology to advance biomedical research.[1,2] Identifying specific cell types provides insights into the early stages of disease progression, thereby aiding the development of targeted therapeutic strategies.[3–5] Over the past two decades, cancer cells have been widely used to study the role of microenvironments within cells.[6–10] However, the study of residential macrophages in the central nervous system (CNS), specifically human microglia, remains largely unexplored.[11–13] Microglia, fast-responsive macrophage cells, play a crucial role to maintain cellular homeostasis.[14] Upon pathogenesis, microglia are rapidly activated, become motile, and secrete inflammatory cytokines. Furthermore, they migrate to lesion sites to clear apoptotic cells, damaged neurons, and cellular debris in response to injury or infection.[14–16] They respond quickly, activate, and degrade foreign substances using hydrolytic enzymes directly controlled by lysosomes.[17,18] This enzymatic biochemical reaction is crucial, and the pH of the lysosomal environment is a primary factor affected during the process.[16,18] Majumder *et al.* reported that the shift from a resting to an activated state of microglia results in a lowering in lysosomal pH.[17,19] Furthermore, under more stressful conditions, this pH reduction becomes even more pronounced.[18–20] Therefore, investigating lysosomal pH in activated microglia is of utmost importance.

β-amyloid (Aβ) peptides, cleaved from amyloid precursor protein during inflammation, can aggregate into insoluble fibrils (fAβ) that form extracellular plaques in the brain and create pH imbalance. These plaques disrupt cellular communication and trigger neuroinflammation, contributing to the progression of Alzheimer's disease.[21–24] Microglia, in their

[a] Molecular Sensors and Therapeutics (MST) Research Laboratory, Department of Chemistry, School of Natural Sciences, Shiv Nadar Institution of Eminence (SNIoE), Delhi NCR, Greater Noida, Uttar Pradesh 201314, India. E-mail: animesh.samanta@snu.edu.in
[b] Department of Life Sciences, School of Natural Sciences, Shiv Nadar Institution of Eminence (SNIoE), Delhi NCR, Greater Noida, Uttar Pradesh, 201314, India
† Present Address: Laboratory of Redox Biology and Metabolism, The Scintillon Research Institute, San Diego, CA, 92121, USA.

resting state, struggle to efficiently degrade foreign substances by lysosomal enzymes due to the relatively high pH.[18,24,25] However, internalized β-amyloid activates microglia, leading to the expression of inflammatory cytokines and lowering the lysosomal pH, thereby enabling microglia to degrade β-amyloid more effectively.[18,26] Therefore, enhancing the clearance of fAβ by activating microglia and subsequently lowering the lysosomal pH could potentially slow the progression of the disease.[23,24,26,27]

In 2018, the International Agency for Research on Cancer authenticated Human Microglia Clone 3 (HMC3) as a standard immortalized human microglial cell line that has been extensively used in neuroscience and neurodegeneration research.[28] Hence, in our study we also use HMC3 cells to study lysosomal pH changes during activation.[19] As functional fluorophores are the most promising imaging agents for mapping pH in the cell to cellular organelles,[29–32,37,38] we develop a lysosome specific pH probe. Although several lysosome specific pH probes have been reported to date, there is still a need to improve their water solubility and optical properties in aqueous media.[33–36,39–41] Therefore, we plan to incorporate a morpholine motif known for specifically targeting lysosomes[42–47] into our indigenous "IndiFluors", which is highly soluble in water along with excellent quantum yields. Herein, we reported the mono-morpholine-tagged **PS-Mor** and di-morpholine tagged **PM-DMor** (Fig. 1) to elucidate the organelle's specificity and pH response. Both morpholine ligands play a crucial role in tuning the emission response through weak and strong photoinduced electron transfer (PET) processes under acidic conditions. Notably, **PS-Mor** and **PM-DMor** exhibit pH-dependent turn-on fluorescence at 562 and 588 nm, respectively, triggered by protonation in acidic environments. This behaviour is further supported by TD-DFT/PCM quantum chemical calculations. Interestingly, **PS-Mor** specifically targets mitochondria in both resting and activated states of microglia, whereas **PM-DMor** exclusively localizes to lysosomes in activated microglia, while localizes mitochondria in the resting state. Furthermore, **PM-DMor** effectively distinguishes between resting and activated HMC3 cells using confocal fluorescence microscopy and FACS analysis. It also monitors microglial activation during β-amyloid internalization by mapping lysosomal pH following phagocytosis.

Results and discussion

Design and synthetic demonstration

To effectively distinguish cellular phenotypes, intracellular pH, particularly lysosomal pH is a critical parameter. In activated HMC3, a decrease in lysosomal pH is a key hallmark, making lysosome-specific pH probes valuable for identifying activation states. To develop organelle specific fluorescence probes, different specific ligands have been utilized.[48–51] For example, weakly basic ligands such as tertiary amines and morpholine are commonly employed for lysosomal targeting.[43,44,46,47] However, the morpholine-ligand does not alone decide specific localization of lysosomes as reported earlier in cancer cells.[52] Thus, we have designed mono- and di-morpholine tagged fluorescent probes, **PS-Mor** and **PM-DMor**, based on pyrylium and pyridinium core scaffolds, respectively (Fig. 1 and Schemes S1 and S2).[48] As the number of morpholine units increases, lipophilicity (log *P*) also increases significantly calculated using the SwissADME tool.[47,48] According to the SILICOS-IT method, the calculated log *P* values are 4.32 for the parent compound (no morpholine), 5.72 for the mono-morpholine derivative, and 7.16 for the di-morpholine derivative.[53,54] First, **PS-Mor** (3,11-dimethoxy-7-(4-morpholinophenyl)-5,6,8,9-tetrahydrodibenzo[*c*,*h*]xanthen-14-ium) was synthesized using 6-methoxy-tetralone and 4-morpholino benzaldehyde in the presence of a $HClO_4$ catalyst with 72% yield (Scheme S1). The probe **PM-DMor** (3,11-dimethoxy-14-(2-morpholinoethyl)-7-(4-morpholinophenyl)-5,6,8,9-tetrahydrodibenzo[*c*,*h*]acridin-14-ium) was synthesized by conjugating the **PS-Mor** with lipophilic 4-(2-aminoethyl)-morpholine, at 60 °C with 68% yield (Scheme S2). All the molecules were characterized by ^{1}H and ^{13}C NMR and HRMS.

Photophysical study

One of the key criteria for an effective fluorescent probe in bioimaging is good aqueous solubility. While several probes exhibit excellent optical properties in organic solvents, they

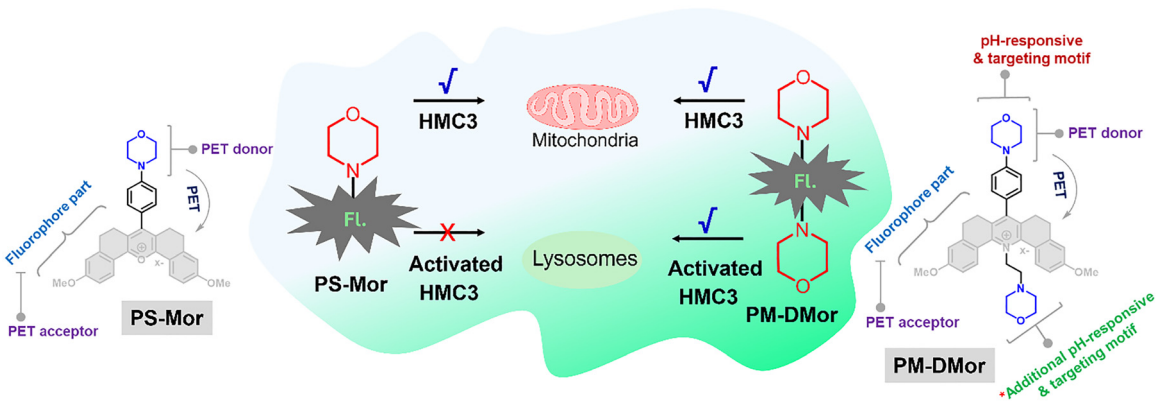

Fig. 1 Schematic representation of the different organelle targeting ability of the **PS-Mor** and **PM-DMor** probes (designed by incorporating the morpholine unit) in human microglia cell state phenotypes.

often fail to perform similarly under physiological conditions due to poor water solubility.[35,55] Our probe **PM-DMor** was highly soluble at lysosomal pH (~4.5) and physiological pH (~7.4) as it shows a linear absorbance at 425 nm until 100 μM with R^2 value 0.999 and 0.999, respectively (Fig. 2a, b and Fig. S1). The spectroscopic properties including absorbance and emission, pH titration, and solubility were evaluated in 10 mM PBS buffer solution with 0.1% DMSO as a co-solvent.

In the pH titration, **PM-DMor** and **PS-Mor** both exhibited an intense emission at 588 nm and 562 nm in acidic pH, whereas it is weakly fluorescent at physiological pH 7.4 (Fig. S3 and S5) with the pK_a value 3.5 ± 0.18 and 3.5 ± 0.02, respectively (Fig. 2d and Fig. S3b). The larger Stokes shifts of **PS-Mor** (>70 nm; Fig. S4) and **PM-DMor** (163 nm; Fig. 2c), respectively, make them excellent candidates for bioimaging by minimizing interference from the excitation light source. Notably, **PM-DMor** exhibits a good quantum yield of 17% in PBS buffer at acidic pH, indicating its high sensitivity for lysosomal imaging. It is well documented that lysosomal pH can decrease under certain pathological conditions, such as neurodegenerative disorders, often reaching values closer to the probe's pK_a (~3.5).[56–58] Our probe exhibits a "turn-on" fluorescence response in acidified lysosomes, as evident from the zoomed-in image in Fig. 2d and Fig. S5. Although the pK_a of the probe is approximately 3.5, the fluorescence activation begins at pH 5.0, indicating its sensitivity to subtle pH shifts in the acidic lysosomal range.

Upon protonation of both morpholine units, **PM-DMor** exhibits a 'turn-on' fluorescence, reaching maximum intensity at pH 3.0 within 35 seconds from pH 7.4 (Fig. 2e). Moreover, **PM-DMor** retains fluorescence even after five pH cycles between 7.4 and 3.0, enabling real-time, reversible pH monitoring in cells (Fig. 2f). Selectivity against metal ions, anions, reactive species, amino acids, and bio-thiols at physiological pH confirmed that only H^+ influences its signal (Fig. S7). It also demonstrates good photostability in PBS under continuous irradiation with a 450 W mercury lamp for 15 minutes (Fig. S6). Thus, **PM-DMor** is a promising probe for tracking intracellular pH fluctuations (ΔpHi).

Theoretical prospects of optical properties

The optical property of the probe has been explained with the help of density functional theory (DFT) at the B3LYP/6-311G(d,p) level through the polarizable continuum model (PCM), considering water as a solvent, using the Gaussian 09 program. The optimized ground state structures of the molecules were confirmed with no imaginary frequencies. The time-dependent density functional theorem (TD-DFT) was employed for the vertical excitation (absorption) by the corrected linear response (cLR) method using the non-equilibrium solvation (PISALR) model. The 'turn on' emission property of the probe can be explained by the manifestation of the double protonation process from neutral/basic form (**PM-DMor**) to acidic form (**PM-DMor2H$^+$**) depicted in Fig. 3a. For better understanding about the emission property, the frontier molecular orbital energy calculation was performed in the G. S. and E. S. for the probe **PM-DMor**. Here, a clear charge transfer state was observed in the S1 state for **PM-DMor**, which was due to the transition from the highest occupied molecular orbital (HOMO) to the lowest unoccupied molecular orbital (LUMO) (Fig. 3a).

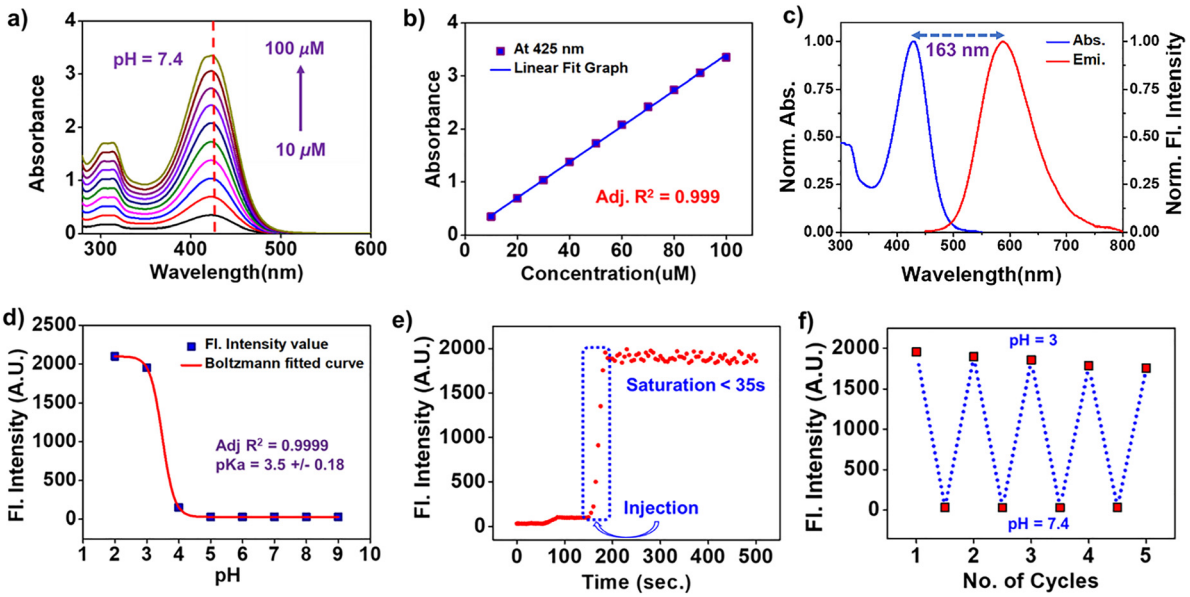

Fig. 2 (a) Concentration dependent UV-vis absorption spectra of **PM-DMor** in PBS buffer at pH 7.4 under ambient conditions to verify no self-aggregation in the concentration range starting from 10 μM to 100 μM. (b) The linear plot (Adj. R^2 value of the linear fitted graph is 0.999) of absorbance at a particular wavelength of 425 nm against the concentration of **PM-DMor** in PBS buffer at pH 7.4, suggesting no self-aggregation and good water solubility. (c) Stokes shift is 163 nm (absorbance and emission at 425 and 588, respectively) of **PM-DMor**. (d) Secondary plot of fluorescence intensity at 588 nm when excited at 425 nm. By Boltzmann curve fitting in Origin pro software, pK_a was determined as 3.5 ± 0.18. (e) Fluorescence response time of **PM-DMor** upon addition of the adjusted amount of acid for pH 7.4–3.0. (f) Reversibility of the fluorescence intensity between pH 3.0 and 7.0.

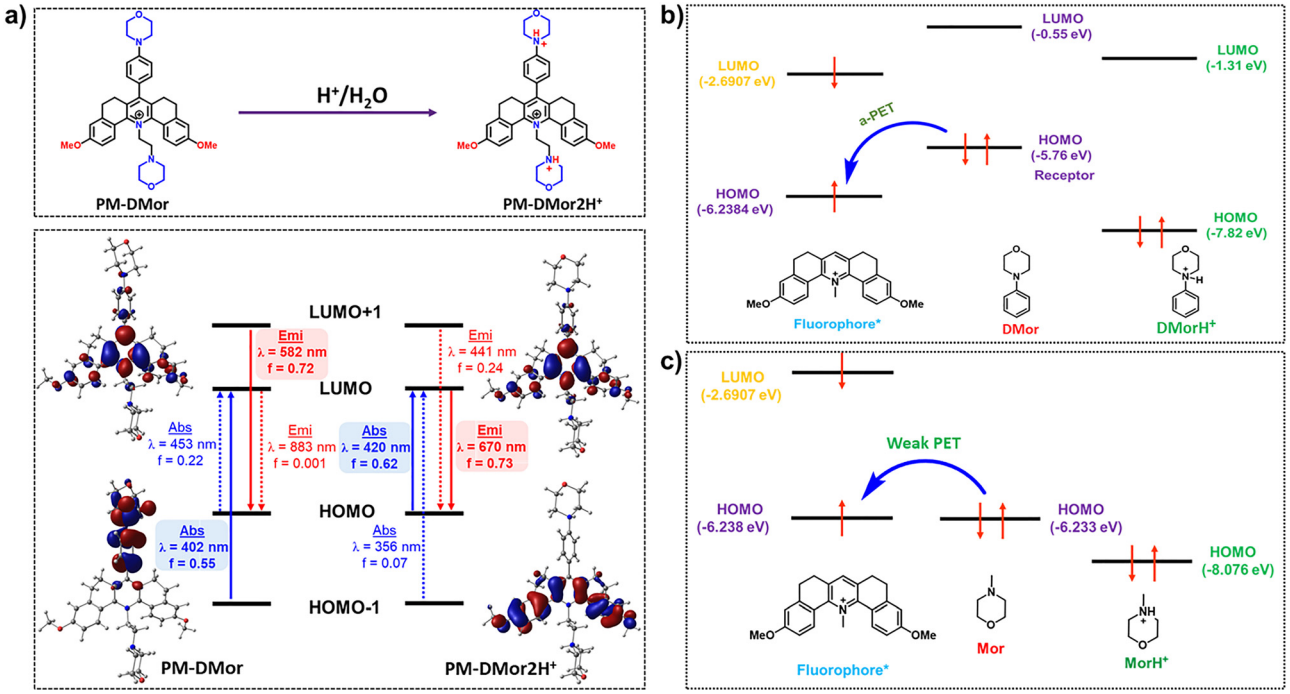

Fig. 3 (a) Theoretical nodal patterns of the frontier pi-MOs and HOMO–LUMO energy diagram of **PM-DMor** and **PM-DMor2H$^+$** (protonated form of **PM-DMor**) along with the simulated absorbance maximum and oscillator strength (f) calculated at the B3LYP/6-311++G(d,p)/PCM level of theory. The theoretical representation of the mechanistic understanding the (b) a-PET and (c) weak PET process for the **PM-DMor** probe.

As shown in Fig. 3a, the HOMO was predominantly located on the **DMor** moiety and the LUMO was located on the fluorophore moiety. The probe shows non-fluorescent property, due to the negligible overlapping area in between the HOMO and LUMO with a low oscillator strength of 0.22. Meanwhile, the role of the additional morpholine (**DMor**) moiety, attached to the fluorophore core, was examined by analysing the frontier molecular orbital energies. The HOMO of the **DMor** moiety (−5.76 eV) lies above the HOMO of the fluorophore core (−6.23 eV) (Fig. 3b), facilitating an efficient photoinduced electron transfer (PET) process, which leads to fluorescence quenching.

In contrast, the role of the morpholine (**Mor**) unit attached to the fluorophore (Fig. 3c) was also evaluated. The HOMO energy levels of both the **Mor** moiety and the fluorophore are almost the same (−6.23 eV), indicating a weak PET process that contributes only partially to fluorescence quenching. In acidic pH, the HOMO energy of the protonated **DMorH$^+$** and **MorH$^+$** moiety decreased to −7.82 eV and −8.07 eV, respectively (Fig. 3b and c). Hence, PET processes are not feasible. The localized electron density was found in both the HOMO and LUMO of the core fluorophore in **PM-DMor2H$^+$** with high oscillator strength of 0.62 (Fig. 3a). Hence, **PM-DMor2H$^+$** exhibited strong fluorescent enhancement by suppressing the PET process.

Cytotoxicity

The biocompatibility of our probes was confirmed through an MTT (methyl thiazolyl tetrazolium) assay in HMC3 cells for 24 hours, which exhibited good viability at the concentrations used for cellular experiments (Fig. S9a–d).

Effect of the morpholine unit in resting HMC3 cells

The effect of the morpholine unit in resting HMC3 cells was determined in cellular colocalization experiments with both **PS-Mor** and **PM-DMor** probes along with LysoTracker deep red (LTDR) and MitoTracker deep red (MTDR). As illustrated in Fig. 4, the merged image of the **PS-Mor** in the green channel with MTDR and in the red channel with LTDR exhibited Pearson's correlation coefficient '*r*' values of 0.92 and 0.33, respectively, indicating that **PS-Mor** is specific to mitochondria. However, the colocalization of **PM-DMor** with MTDR and LTDR showed '*r*' values of 0.52 and 0.48, respectively, suggesting that **PM-DMor** is nonspecific to either mitochondria or lysosomes. In the zoomed-in images, **PS-Mor** shows strong colocalization with mitochondria, as its positive charge facilitates interaction with the negatively charged mitochondrial membrane potential, consistent with a previous report.[52] In contrast, **PM-DMor** exhibits partial localization in both mitochondria and lysosomes. This difference may be attributed to the presence of two basic morpholine units in **PM-DMor**, which favour interaction with the acidic and lipophilic lysosomal environment.

Effect of the morpholine unit in activated HMC3

It is widely recognized that microglial cells can be activated through various intrinsic and extrinsic signaling pathways.[16,59,60] Microglia, despite containing high levels of lysosomal proteases, possess less acidic lysosomes, which reduces the enzymatic efficiency required for effective pathogen degradation.[60–63] Studies show that HMC3 cells treated with LPS/IFNγ enter an activated state, producing pro-inflammatory cytokines,

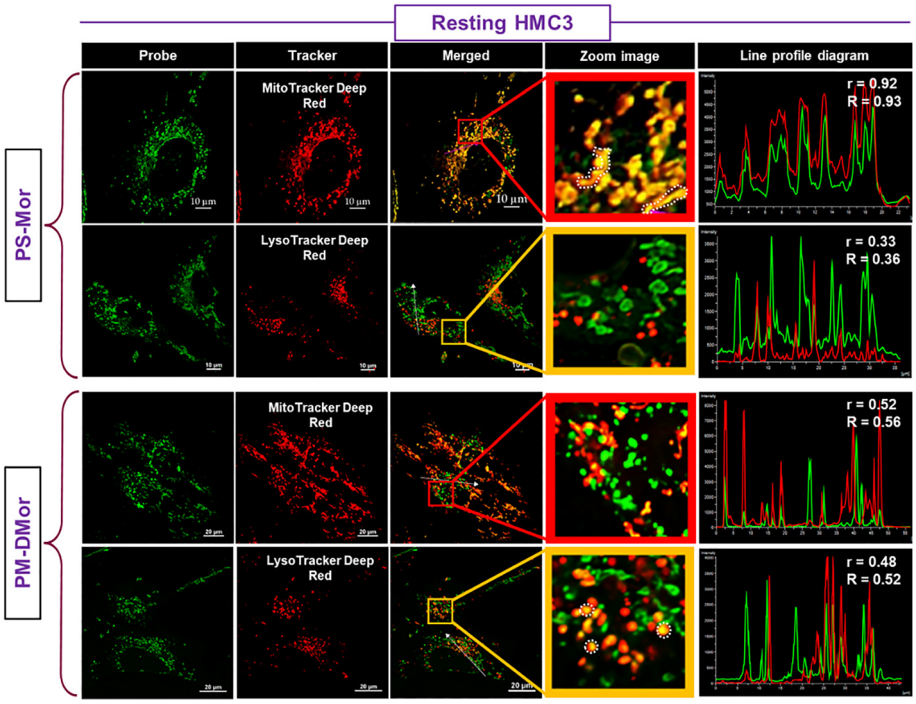

Fig. 4 Confocal fluorescence images for intracellular co-localization in the green channel (em. 550–600 nm, ex. 488 nm) of **PS-Mor** (10 μM) and **PM-DMor** (10 μM) after administration in HMC3 cells for 30 min. Images were taken after counterstaining with MitoTracker deep red (100 nM) and LysoTracker deep red (100 nM) in the red channel (em. 650–720 nm, ex. 640 nm), respectively. The line profile diagram of the merged images is shown by the arrow marks. Here, '*r*' and '*R*' represent Pearson's correlation coefficient and Mander's overlap coefficient, respectively. Images were captured using a 60× oil emersion lens with 2× zoom.

acidifying the lysosomes, and enhancing the phagocytotic-fusion of pathogenic substances.[16,61,62] We also conducted co-localization confocal image analysis in the activated human microglia (HMC3) cells for both the probes, **PS-Mor** and **PM-DMor**. As shown in Fig. 5a and b, the merged fluorescence images of the green and red channels reveal strong colocalization of **PS-Mor** with the mitochondrial tracker (MTDR), yielding a high Pearson's correlation coefficient of 0.92, while showing minimal overlap with the lysosomal tracker (LTDR; 0.26). This confirms the selective mitochondrial localization of **PS-Mor** in activated HMC3 cells. In contrast, **PM-DMor** exhibits a high Pearson's coefficient of 0.92 with LTDR and a much lower value of 0.30 with MTDR, indicating its predominant localization in lysosomes (Fig. 5a and b). The enhanced lysosomal targeting of **PM-DMor** in the activated state, compared to the resting state, can be attributed to its structural design incorporating two morpholine units. These basic morpholine moieties mimic the lysosomal lipophilic and acidic environment and undergo protonation, facilitating their selective accumulation in lysosomes *via* lysosomotropism. Overall, the incorporation of a second morpholine unit into the fluorophore framework led to the successful development of a lysosome-specific fluorescent probe (**PM-DMor**) for activated HMC3 cells. To assess further the discrimination of phenotypes in HMC3 cells of our lysosomal specific pH-responsive probe, **PM-DMor**, we conducted a fluorescence-activated cell sorting (FACS) experiment. As depicted in Fig. 5c, a significant enhancement in fluorescence intensity was observed in LPS/IFNγ-treated activated HMC3 cells after 24 hours of treatment, compared to untreated resting HMC3 cells. This observation supports the notion that the pH-responsive fluorescent probe, **PM-DMor**, has the potential to successfully discriminate the state of microglia by targeting different cellular organelles.

pH-monitoring in externally stimulated HMC3

While **PM-DMor** specifically targets lysosomes in activated microglia, it remains to be explored whether the probe can effectively monitor intracellular pH changes in response to external stimuli that cause apoptosis. Various anticancer drugs that induce apoptosis can cause intracellular pH changes.[64–67] Cisplatin, a longstanding chemotherapy drug, has an unclear biochemical mechanism. It induces cancer cell death through apoptosis or necrosis by binding to DNA and changes the cell's metabolic state.[68] Additionally, lipopolysaccharide (LPS) promotes apoptosis primarily through TNF-α production in the early stages and nitric oxide in the later stages.[69] On the contrary, chloroquine, a well-known anti-malarial drug, can stimulate the living cells by increasing the pH of the lysosome.[65] Overall, changes in intracellular pH are consistently observed during treatment with these agents. To assess lysosomal pH imbalances in HMC3 cells upon external drug stimulation, cells were treated individually with lipopolysaccharide (LPS, 1 μg mL^{-1}), cisplatin (10 μM), or chloroquine (100 μM) for 12 hours. Following treatment, the cells were incubated with

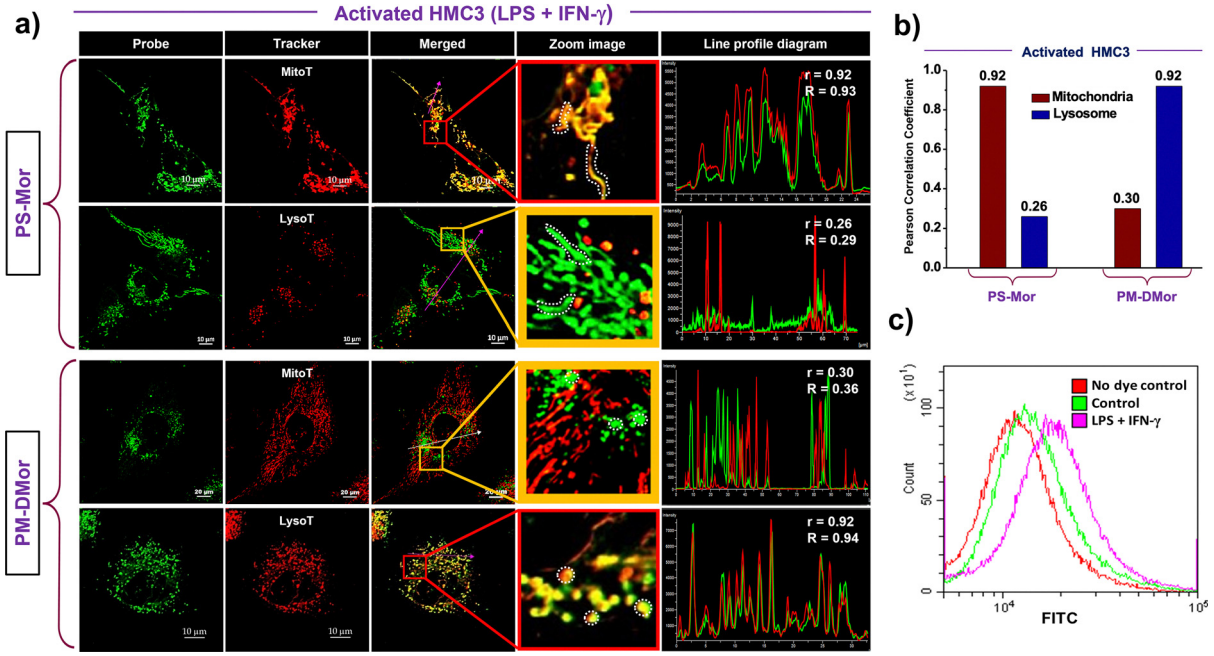

Fig. 5 (a) Confocal fluorescence images for intracellular co-localization in the green channel (em. 550–600 nm, ex. 488 nm) of **PS-Mor** (20 μM) and **PM-DMor** (20 μM) after administration in HMC3 cells for 30 min. Images were taken after counterstaining with MitoTracker deep red (100 nM) and LysoTracker deep red (100 nM) in the red channel (em. 650–720 nm, ex. 640 nm), respectively. The line profile diagram of the merged images is shown by the arrow marks. Here, '*r*' and '*R*' represent Pearson's correlation coefficient and Mander's overlap coefficient, respectively. Images were captured using a 60× oil emersion lens with 2× zoom. (b) Comparable Pearson correlation coefficient of the merged images of lysoT and mitoT with **PS-Mor** and **PM-DMor**. (c) FACS analysis to discriminate the HMC3 cell state by **PM-DMor**. Here, the line spectra correspond to the representative color; red: no treatment + no dye, green: no treatment + dye, violet: LPS + IFN$_\gamma$ treatment + dye.

the lysosome-targeting pH-sensitive fluorescent probe **PM-DMor** (10 μM) at 37 °C for 15 minutes. Fluorescence imaging was then performed using the green channel (excitation: 480 nm; emission: 550–600 nm).

As shown in Fig. 6a and b and Fig. S10, cells treated with LPS or cisplatin exhibited a significant increase in fluorescence intensity, indicative of enhanced lysosomal acidification typically associated with apoptotic processes. In contrast, chloroquine-treated cells showed a marked decrease in fluorescence intensity, consistent with elevated lysosomal pH due to the alkalinizing effect of chloroquine. Note that the representative lysosomal regions are highlighted in the images to visually emphasize the

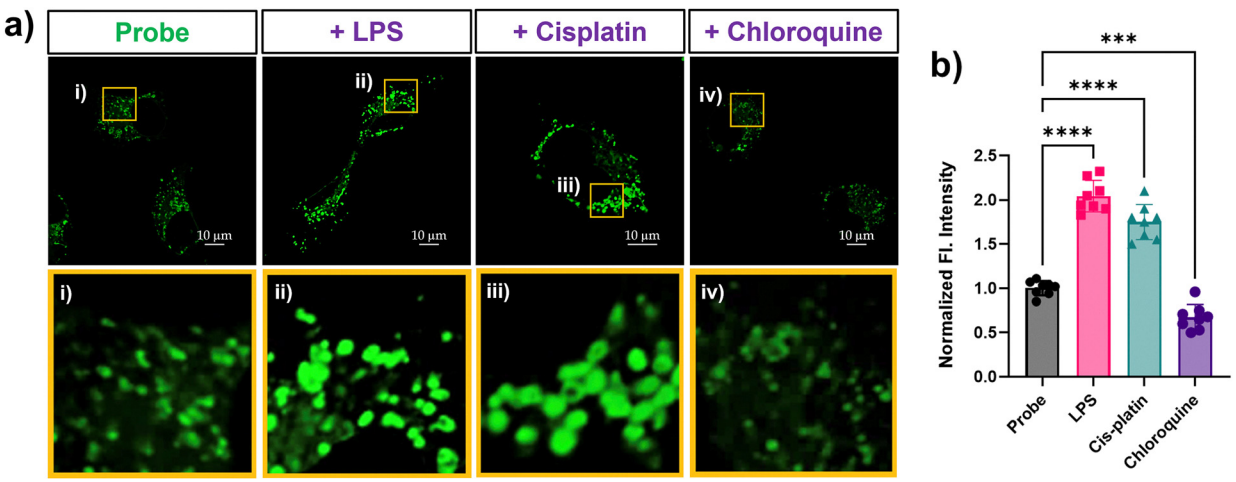

Fig. 6 (a) Fluorescence images for HMC3 cells during the external stimuli condition. Cells were administered with **PM-DMor** (10 μM) and images were taken in the green channel after incubation of different stimuli. Lysosomal regions were highlighted by white dotted circular lines. The image scale bar is 10 μm. (b) Normalized fluorescence intensity of the HMC3 cells during the Lipopolysaccharide and cisplatin and chloroquine treatment condition. Data represents the means ± SEM (n = 8). *Shows significant values compared to control, with a p-value, ***$p \leq 0.001$, ****$p \leq 0.0001$. Statistical significance was calculated using an ANOVA test.

changes in fluorescence intensity, with punctate fluorescent spots confirming lysosomal localization of the **PM-DMor** probe. These results further support the potential of the **PM-DMor** probe as a candidate for lysosomal pH measurement.

Furthermore, **PM-DMor**'s ability to monitor pH changes during apoptosis was evaluated in HMC3 cells treated with 200 μM H_2O_2. Apoptosis was first confirmed using Annexin V and propidium iodide (Fig. S11a). Cells were then treated with H_2O_2, followed by incubation with **PM-DMor** for 15 minutes, and fluorescence images were acquired (Fig. S11b and c). A significant increase in fluorescence intensity was observed compared to the control, indicating pH modulation during apoptosis. The probe's morpholine moiety facilitates lysosomal targeting at low pH, making **PM-DMor** a promising tool for tracking lysosomal acidification and apoptosis.

Illumination of β-amyloid induced activated HMC3 by PM-DMor

Under both intrinsic and extrinsic stimuli, HMC3 cells can be activated, resulting in the expression and secretion of several pro-inflammatory cytokines as part of the primary host defence against various pathogens.[70] Either we can measure these cytokines to confirm activation or we can also use a simpler method by checking lysosomal pH. To induce activation and promote a pro-inflammatory phenotype in HMC3 cells, we treated them overnight with β-amyloid, with or without LPS, in culture. As shown in Fig. 7, the Pearson's correlation coefficients for the merged images of **PM-DMor** and LysoTracker were 0.79 (β-amyloid), 0.76 (LPS) and 0.90 (β-amyloid + LPS) under different activation conditions. These high correlation values indicate clear lysosomal localization of **PM-DMor** and confirm the successful pro-inflammatory activation of HMC3 cells. β-Amyloid can activate microglia, leading to a decrease in intracellular pH, which facilitates lysosomal digestion of β-amyloid in both its soluble and fibrillar forms.[71] As our probe **PM-DMor** is capable of illuminating the phenotypes of microglial dynamics by mapping lysosomal pH, it is also useful to study the phagocytosis of *β*-amyloid.

Phagocytosis of β-amyloid in activated HMC3

In Alzheimer's disease, β-amyloid activates microglia, promoting pro-inflammatory cytokine release and lysosomal acidification for fibril clearance (Fig. 8a). However, under less acidic lysosomal conditions, microglial clearance of β-amyloid is reduced. Here, we employed our lysosome-specific pH probe, **PM-DMor**, to monitor phagocytosis of β-amyloid in resting and activated HMC3 cells through confocal microscopy imaging.

To study the lysosomal fusion with phagocytotic particles, a phagocytotic marker, pHrodo-Red *E. coli*-conjugated bioparticles (*E. coli P*) were treated with HMC3 cells, which had been previously activated by the administration of β-amyloid for 24 hours. As shown in Fig. 8c and d, β-amyloid-treated HMC3 cells exhibit a significant decrease in lysosomal pH, indicating increased acidity, as mapped by **PM-DMor**. This acidification is correlated with cell activation and is accompanied by enhanced uptake of fluorescent *E. coli* particles at the single-cell level, compared to non-treated cells (Fig. 8b). Herein, as depicted in Fig. 8e(ii), to track the lysosome, LysoTracker deep red (LysoT) was also administered along with **PM-DMor** (probe) in β-amyloid treated HMC3. As shown in Fig. 8e(i, ii and iii) and

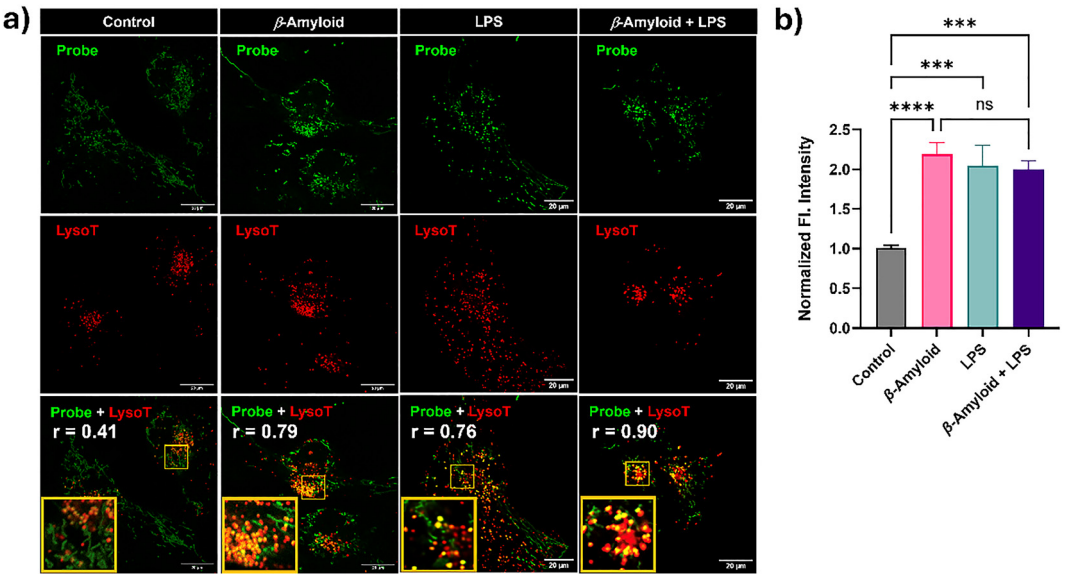

Fig. 7 (a) Confocal fluorescence images for intracellular localization study of the **PM-DMor** probe. Here, HMC3 cells were administered with probe that was previously treated with either β-amyloid, LPS alone or β-amyloid + LPS. For labeling lysosomes, the cells were also treated with LysoTracker deep red, and images were taken in different channels and the corresponding merged image was represented with "*r*" (Pearson's correlation coefficient) values. The image scale bar is 20 μm. Images were captured using a 60× oil emersion lens with 2× zoom. (b) Normalized fluorescence intensity of the HMC3 cells at different treatment conditions of the representative (a). Data represents the mean ± SD of three independent experiments. *Shows significance values compared to the control, with a *p*-value, ****$p \leq 0.0001$, ***$p = 0.0001$, ***$p = 0.0002$, ns = 0.5439, respectively. Statistical significance was calculated using a one-way ANOVA test.

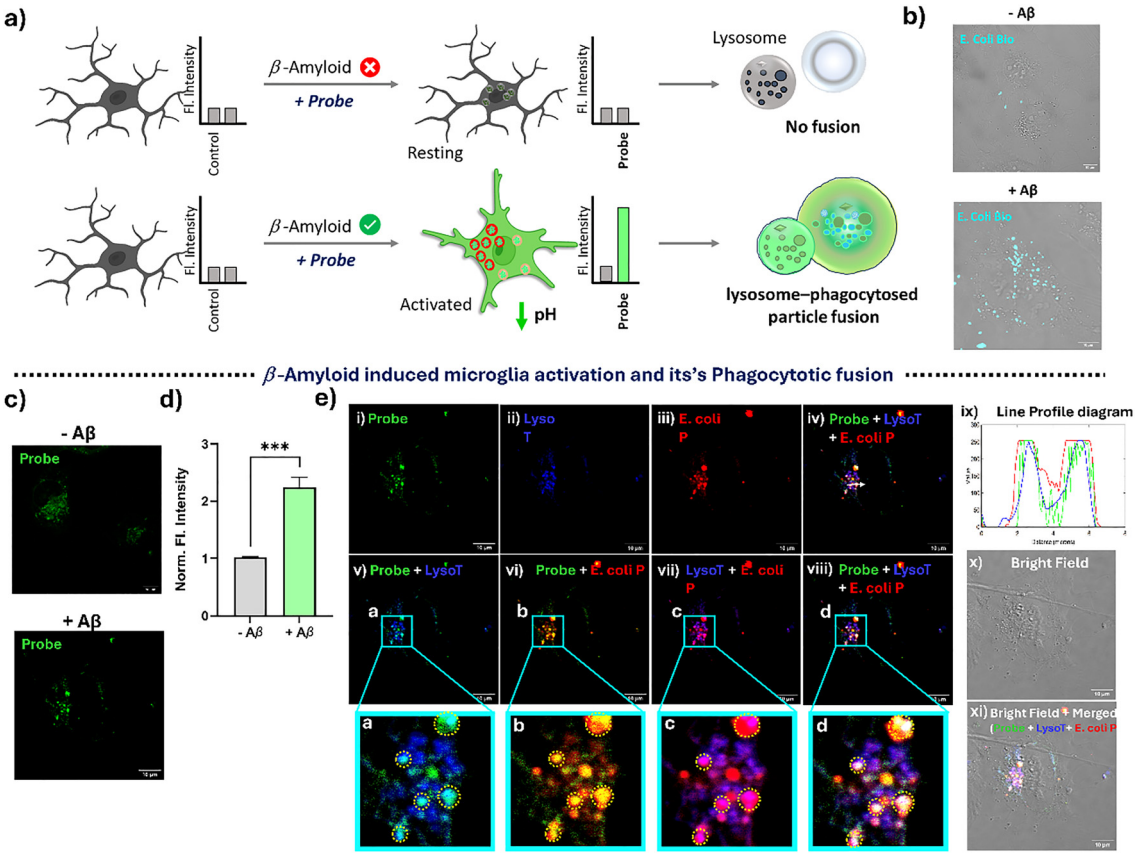

Fig. 8 (a) Schematic representation of the **PM-DMor** probe in tracking lysosomal pH changes (during β-amyloid treatment) by focusing on the lysosome-phagocytosed particle fusion. β-Amyloid-induced phagocytotic engulfment towards (b) pHrodo-Red *E. coli*-bioparticles (marked as pseudocolor; red channel 620–650 nm, ex. 560 nm), and (c) probe **PM-DMor** (green channel, em. 550–600 nm, ex. 488 nm). (d) Normalized fluorescence intensity of the probe in the absence and presence of β-amyloid treatment. The image scale bar is 10 μm. Images were captured using a 60×oil emersion lens with 2× zoom. Data represents mean ± SD of three independent experiments. *Shows significance values compared to control, with a *p*-value, ***p = 0.0003. Statistical significance was calculated using an unpaired *t*-test. (e) β-Amyloid-induced HMC3 activation and its phagocytotic fusion. Confocal fluorescence images for pH-tracking during β-amyloid-fusion, tracked by (i) **PM-DMor** probe; (ii) LysoTracker deep red; (iii) pHrodo-Red *E. coli*-bioparticles; (iv) overlap images of (i), (ii), and (iii); (v) overlap images of (i) and (ii); (vi) overlap images of (i) and (iii); (vii) overlap images of (ii) and (iii); (viii) overlap images of (i), (ii), and (iii); (ix) line profile diagram for colocalization study; and (xi) overlap images of (x) & (iv).

their overlapping images in Fig. 8e(v, vi, vii and viii), we obtained clear overlapping images of the **PM-DMor** with LysoT and *E. coli P*. Moreover, the zoomed-in images in Fig. 8e(viii; d) further confirmed the initiation of phagocytosis. In conclusion, our findings provide valuable insights into the phagocytotic-fusion during the β-amyloid internalization in HMC3 cells. This novel approach can potentially serve as a valuable tool for future studies investigating the mechanisms of accumulation of β-amyloid in brain cellular models. Most importantly, the probe may be useful to screen drugs for therapeutics targeting phagocytotic β-amyloid-fusion, through monitoring lysosomal acidity.

Conclusions

We have developed two pH-responsive fluorescent probes: **PS-Mor**, tagged with a single morpholine unit, and **PM-DMor**, tagged with two morpholine units. **PS-Mor** localizes specifically to mitochondria in both resting and activated HMC3 cells. In contrast, **PM-DMor** selectively targets lysosomes only in activated microglia. This lysosomal localization is attributed to the presence of two basic morpholine groups, which better mimic the lipophilic and acidic lysosomal environment. The dual morpholine units allow **PM-DMor** to outcompete the mitochondrial targeting seen with **PS-Mor**, which is influenced by the negative mitochondrial membrane potential. The morpholine unit is pivotal in controlling the pH-responsive property through the photoinduced electron transfer (PET). Photophysical studies clearly suggest that **PM-DMor** enables real-time monitoring of lysosomal pH change (ΔpHi) in HMC3. Despite **PM-DMor**'s pK_a shortcomings falling slightly below the typical pH window of 4.5–6.0, this feature is advantageous for specifically targeting lysosomes in activated macrophages, favouring acidic pH in drug-induced cellular stress conditions. Moreover, we investigated pH imbalances during apoptosis and different drug-induced cellular stress conditions, such as lipopolysaccharide, cisplatin, and chloroquine. Additionally, **PM-DMor**

was found to be effective to discriminate HMC3 cell states through fluorescence microscopy and FACS analysis. β-Amyloid accumulation activates microglia, leading to increased lysosomal acidity that facilitates β-amyloid-fusion through phagocytosis. **PM-DMor** shows promise as a fluorescent marker for distinguishing HMC3 cell phenotypes and for screening drugs that enhance lysosomal acidification, a process potentially regulated by microglial activity in Alzheimer's disease.

Author contributions

S. M. and A. S. conceived the idea for the project and wrote the original draft of the work, followed by data curation, funding acquisition, formal analysis, investigation, project administration, and validation, with the assistance of the other authors, A. M., S. T., R. Y., and N. P.

Conflicts of interest

There are no conflicts to declare.

Data availability

The data supporting this article have been included within the manuscript as well as in the SI. Supplementary information: Details of the materials and methods; synthesis schemes; experimental procedures; results and discussion; cellular studies; characterization of the molecules; and catalog of Cartesian coordinates. See DOI: **https://doi.org/10.1039/d5tb00968e**.

Acknowledgements

A. S. is grateful to the DST-SERB, India, for the DST-Core Research grant (CRG/2021/002313) and to the Shiv Nadar Foundation (SNF) grant (Collab0007) for funding. PhD students S. M., A. M., R. Y. and N. P. are grateful to Shiv Nadar Institution of Eminence (SNIoE), Delhi NCR, and the Shiv Nadar Foundation for their research fellowships. S. T. is grateful to Shiv Nadar Institution of Eminence (SNIoE) for her B.Sc. (Research) final year project (FYP). The authors acknowledge the SNIoE, DST-FIST grant for the confocal microscopy and DST-FIST MALDI facility (Sanction Order No. SR/FST/CS-I/2017/13(C)) at Shiv Nadar Institution of Eminence, Delhi NCR. The authors are thankful to the high-performance cluster computing (HPC) facility (MAGUS) of Shiv Nadar Institution of Eminence (SNIoE), Delhi NCR. Department of Life Science, Shiv Nadar Institution of Eminence (SNIoE) is gratefully acknowledged for helping us in various ways.

References

1 A. M. Jurga, M. Paleczna and K. Z. Kuter, *Front. Cell. Neurosci.*, 2020, **14**, 1–18.
2 A. Lamiable, T. Champetier, F. Leonardi, E. Cohen, P. Sommer, D. Hardy, N. Argy, A. Massougbodji, E. Del Nery, G. Cottrell, Y. J. Kwon and A. Genovesio, *Nat. Commun.*, 2023, **14**, 6386.
3 A. E. H. El-Kadiry, M. Rafei and R. Shammaa, *Front. Med.*, 2021, **8**, 1–24.
4 J. Guan, Y. Lin, Y. Wang, J. Gao and G. Ji, *J. Transl. Med.*, 2021, **19**, 1–12.
5 K. A. Jagadeesh, K. K. Dey, D. T. Montoro, R. Mohan, S. Gazal, J. M. Engreitz, R. J. Xavier, A. L. Price and A. Regev, *Nat. Genet.*, 2022, **54**, 1479–1492.
6 S. Munan, R. Yadav, N. Pareek and A. Samanta, *Analyst*, 2023, **148**, 4242–4262.
7 M. Vendrell, D. Zhai, J. C. Er and Y. T. Chang, *Chem. Rev.*, 2012, **112**, 4391–4420.
8 N. Pareek, R. Yadav, S. Munan, M. Baruah and A. Samanta, *Chem. – Eur. J.*, 2025, **31**, e202404523.
9 A. Chatterjee, S. Sarkar, S. Bhattacharjee, A. Bhattacharyya, S. Barman, U. Pal, R. Pandey, A. Ethirajan, B. Jana, B. B. Das and A. Das, *J. Am. Chem. Soc.*, 2025, **147**, 532–547.
10 J. H. Lee, K. Kozoriz, K. T. Hong, D. P. Murale, S. J. An, S.-H. Choi and J.-S. Lee, *J. Med. Chem.*, 2025, **68**(10), 9947–9957.
11 K. E. Prater, K. J. Green, S. Mamde, W. Sun, A. Cochoit, C. L. Smith, K. L. Chiou, L. Heath, S. E. Rose, J. Wiley, C. D. Keene, R. Y. Kwon, N. Snyder-Mackler, E. E. Blue, B. Logsdon, J. E. Young, A. Shojaie, G. A. Garden and S. Jayadev, *Nat. Aging*, 2023, **3**, 894–907.
12 S. Munan, A. Mondal, S. Shailja, S. Pati and A. Samanta, *Anal. Chem.*, 2024, **96**, 7479–7486.
13 M. J. Dolan, M. Therrien, S. Jereb, T. Kamath, V. Gazestani, T. Atkeson, S. E. Marsh, A. Goeva, N. M. Lojek, S. Murphy, C. M. White, J. Joung, B. Liu, F. Limone, K. Eggan, N. Hacohen, B. E. Bernstein, C. K. Glass, V. Leinonen, M. Blurton-Jones, F. Zhang, C. B. Epstein, E. Z. Macosko and B. Stevens, *Nat. Immunol.*, 2023, **24**, 1382–1390.
14 A. M. Rodríguez, J. Rodríguez and G. H. Giambartolomei, *ASN Neuro*, 2022, **14**, 1–15, DOI: **10.1177/17590914221104566**.
15 R. Fu, Q. Shen, P. Xu, J. J. Luo and Y. Tang, *Mol. Neurobiol.*, 2014, **49**, 1422–1434.
16 C. Gao, J. Jiang, Y. Tan and S. Chen, *Signal Transduction Targeted Ther.*, 2023, **8**, 359.
17 R. G. Jacquet, F. González Ibáñez, K. Picard, L. Funes, M. Khakpour, G. K. Gouras, M.-È. Tremblay, F. R. Maxfield and S. Solé-Domènech, *Cell Rep.*, 2024, **43**, 115052.
18 A. Majumdar, D. Cruz, N. Asamoah, A. Buxbaum, I. Sohar, P. Lobel and F. R. Maxfield, *Mol. Biol. Cell*, 2007, **18**, 1490–1496.
19 J. D. Quick, C. Silva, J. H. Wong, K. L. Lim, R. Reynolds, A. M. Barron, J. Zeng and C. H. Lo, *J. Neuroinflammation*, 2023, **20**, 185.
20 K. Schniererová, H. Janeková, J. Joniak, M. Putala, P. Štacko and H. Stankovičová, *Chem. – Eur. J.*, 2024, **30**, e202400111.
21 H. Hampel, J. Hardy, K. Blennow, C. Chen, G. Perry, S. H. Kim, V. L. Villemagne, P. Aisen, M. Vendruscolo, T. Iwatsubo, C. L. Masters, M. Cho, L. Lannfelt, J. L. Cummings and A. Vergallo, *Mol. Psychiatry*, 2021, **26**, 5481–5503.

22 W. Zhang, D. Xiao, Q. Mao and H. Xia, *Signal Transduction Targeted Ther.*, 2023, **8**, 267.
23 M. Dani, M. Wood, R. Mizoguchi, Z. Fan, Z. Walker, R. Morgan, R. Hinz, M. Biju, T. Kuruvilla, D. J. Brooks and P. Edison, *Brain*, 2018, **141**, 2740–2754.
24 M. Gratuze, Y. Chen, S. Parhizkar, N. Jain, M. R. Strickland, J. R. Serrano, M. Colonna, J. D. Ulrich and D. M. Holtzman, *J. Exp. Med.*, 2021, **218**, e20210542.
25 C. K. Combs, J. Colleen Karlo, S. C. Kao and G. E. Landreth, *J. Neurosci.*, 2001, **21**, 1179–1188.
26 X. Zhao, J. Sun, L. Xiong, L. She, L. Li, H. Tang, Y. Zeng, F. Chen, X. Han, S. Ye, W. Wang, X. Wang and G. Liang, *Int. J. Biol. Sci.*, 2023, **19**, 3249–3265.
27 A. Fernandez, M. Vermeren, D. Humphries, R. Subiros-Funosas, N. Barth, L. Campana, A. MacKinnon, Y. Feng and M. Vendrell, *ACS Cent. Sci.*, 2017, **3**, 995–1005.
28 C. Dello Russo, N. Cappoli, I. Coletta, D. Mezzogori, F. Paciello, G. Pozzoli, P. Navarra and A. Battaglia, *J. Neuroinflammation*, 2018, **15**, 259.
29 R. Yadav, S. Munan, V. Kardam, K. Dutta Dubey and A. Samanta, *Chemistry*, 2023, **29**, e202300244.
30 J. Yin, L. Huang, L. Wu, J. Li, T. D. James and W. Lin, *Chem. Soc. Rev.*, 2021, **50**, 12098–12150.
31 J. J. Rennick, C. J. Nowell, C. W. Pouton and A. P. R. Johnston, *Nat. Commun.*, 2022, **13**, 6023.
32 A. Podder, M. M. Joseph, S. Biswas, S. Samanta, K. K. Maiti and S. Bhuniya, *Chem. Commun.*, 2021, **57**, 607–610.
33 S. Chen, T. D. James, A. L. Koner and B. Z. Tang, *J. Mater. Chem. B*, 2025, **13**, 4249–4251.
34 S. I. Reja, M. Minoshima, Y. Hori and K. Kikuchi, *Biosens. Bioelectron.*, 2024, **247**, 115862.
35 M. Liu, J. Weng, S. Huang, W. Yin, H. Zhang, Y. Jiang, L. Yang and H. Sun, *Chem. Commun.*, 2023, **59**, 3570–3573.
36 A. Jana, M. Baruah, S. Munan and A. Samanta, *Chem. Commun.*, 2021, **57**, 6380–6383.
37 S. K. Pramanik, S. Sreedharan, H. Singh, M. Khan, K. Tiwari, A. Shiras, C. Smythe, J. A. Thomas and A. Das, *Bioconjugate Chem.*, 2018, **29**, 3532–3543.
38 R. Tiwari, P. S. Shinde, S. Sreedharan, A. K. Dey, K. A. Vallis, S. B. Mhaske, S. K. Pramanik and A. Das, *Chem. Sci.*, 2021, **12**, 2667–2673.
39 S. K. Pramanik and A. Das, *Chem. Commun.*, 2021, **57**, 12058–12073.
40 R. Tiwari, S. Banerjee, D. Tyde, K. Das Saha, A. Ethirajan, N. Mukherjee, S. Chattopadhy, S. K. Pramanik and A. Das, *Bioconjugate Chem.*, 2021, **32**, 245–253.
41 H. Singh, S. Sreedharan, K. Tiwari, N. H. Green, C. Smythe, S. K. Pramanik, J. A. Thomas and A. Das, *Chem. Commun.*, 2019, **55**, 521–524.
42 S. D. B. Goldman, R. S. Funk, R. A. Rajewski and J. P. Krise, *Bioanalysis*, 2009, **1**, 1445–1459.
43 L.-L. Li, K. Li, M.-Y. Li, L. Shi, Y.-H. Liu, H. Zhang, S.-L. Pan, N. Wang, Q. Zhou and X.-Q. Yu, *Anal. Chem.*, 2018, **90**, 5873–5878.
44 B. Zhang, X. Yang, R. Zhang, Y. Liu, X. Ren, M. Xian, Y. Ye and Y. Zhao, *Anal. Chem.*, 2017, **89**, 10384–10390.
45 M. Ren, Z. Li, B. Deng, L. Wang and W. Lin, *Anal. Chem.*, 2019, **91**, 2932–2938.
46 C. Du, S. Fu, X. Wang, A. C. Sedgwick, W. Zhen, M. Li, X. Li, J. Zhou, Z. Wang, H. Wang and J. L. Sessler, *Chem. Sci.*, 2019, **10**, 5699–5704.
47 Q. Wan, S. Chen, W. Shi, L. Li and H. Ma, *Angew. Chem.*, 2014, **126**, 11096–11100.
48 S. Munan, S. Kottarathil, M. M. Joseph, A. Jana, M. Ali, K. Mapa, K. K. Maiti and A. Samanta, *ACS Sens.*, 2024, **9**, 3502–3510.
49 J. Lin, K. Yang and E. J. New, *Org. Biomol. Chem.*, 2021, **19**, 9339–9357.
50 M. Zhu, W. Li, L. Sun, Z. Lv, X. Yang and Y. Wang, *Coord. Chem. Rev.*, 2024, **512**, 215893.
51 P. Gao, W. Pan, N. Li and B. Tang, *Chem. Sci.*, 2019, **10**, 6035–6071.
52 S. Munan, M. Ali, R. Yadav, K. Mapa and A. Samanta, *Anal. Chem.*, 2022, **94**, 11633–11642.
53 A. Daina, O. Michielin and V. Zoete, *Sci. Rep.*, 2017, **7**, 42717.
54 X. Liu, X. Zhang, Y. Han, X. Li and J. Li, *Chemistry*, 2025, **7**, 82.
55 S. Debnath, R. Ghosh, R. R. Nair, D. Pradhan and P. B. Chatterjee, *ACS Omega*, 2022, **7**, 38122–38149.
56 H. Hagihara and T. Miyakawa, *Int. J. Neuropsychopharmacol.*, 2024, **7**, 10.
57 Y. Decker, E. Németh, R. Schomburg, A. Chemla, L. Fülöp, M. D. Menger, Y. Liu and K. Fassbender, *Neurobiol. Aging*, 2021, **101**, 40–49.
58 Y. Decker, E. Németh, R. Schomburg, A. Chemla, L. Fülöp, M. D. Menger, Y. Liu and K. Fassbender, *Neurobiol. Aging*, 2021, **101**, 40–49.
59 Y.-L. Tan, Y. Yuan and L. Tian, *Mol. Psychiatry*, 2020, **25**, 351–367.
60 M. Colonna and O. Butovsky, *Annu. Rev. Immunol.*, 2017, **35**, 441–468.
61 S. R. Bonam, F. Wang and S. Muller, *Nat. Rev. Drug Discovery*, 2019, **18**, 923–948.
62 S. Müller, J. Dennemärker and T. Reinheckel, *Biochim. Biophys. Acta*, 2012, **1824**, 34–43.
63 J. D. Quick, C. Silva, J. H. Wong, K. L. Lim, R. Reynolds, A. M. Barron, J. Zeng and C. H. Lo, *J. Neuroinflammation*, 2023, **20**, 185.
64 D. Lagadic-Gossmann, L. Huc and V. Lecureur, *Cell Death Differ.*, 2004, **11**, 953–961.
65 P. W. Halcrow, J. D. Geiger and X. Chen, *Front. Cell Dev. Biol.*, 2021, **9**, 627639.
66 S. Simon, D. Roy and M. Schindler, *Proc. Natl. Acad. Sci. U. S. A.*, 1994, **91**, 1128–1132.
67 S. M. Simon, *Drug Discovery Today*, 1999, **4**, 32–38.
68 S. Dasari and P. B. Tchounwou, *Eur. J. Pharmacol.*, 2014, **740**, 364–378.
69 J. Xaus, M. Comalada, A. F. Valledor, J. Lloberas, F. López-Soriano, J. M. Argilés, C. Bogdan and A. Celada, *Blood*, 2000, **95**, 3823–3831.
70 G. A. Duque and A. Descoteaux, *Front. Immunol.*, 2014, **5**, 1–12.
71 M. P. Murphy and H. LeVine 3rd, *J Alzheimers Dis*, 2010, **19**, 311–323.

